Journal of Biomedical Optics

SPIEDigitalLibrary.org/jbo

Differential diagnosis of lung carcinoma with three-dimensional quantitative molecular vibrational imaging

Liang Gao
Ahmad A. Hammoudi
Fuhai Li
Michael J. Thrall
Philip T. Cagle
Yuanxin Chen
Jian Yang
Xiaofeng Xia
Yubo Fan
Yehia Massoud
Zhiyong Wang
Stephen T. C. Wong

SPIE

Differential diagnosis of lung carcinoma with three-dimensional quantitative molecular vibrational imaging

Liang Gao,[a,b*] Ahmad A. Hammoudi,[a,c*] Fuhai Li,[a,e] Michael J. Thrall,[d] Philip T. Cagle,[d] Yuanxin Chen,[a] Jian Yang,[a] Xiaofeng Xia,[a,e] Yubo Fan,[a] Yehia Massoud,[c] Zhiyong Wang,[a] and Stephen T. C. Wong[a,c,d,e]

[a]Cornell University, The Methodist Hospital Research Institute, Weill Cornell Medical College, Department of Systems Medicine and Bioengineering, Houston, Texas 77030
[b]Chroma Technology, 10 Imtec Lane, Bellows Falls, Vermont 05101
[c]Rice University, Department of Electrical and Computer Engineering, Houston, Texas 77005
[d]Cornell University, Weill Cornell Medical College, The Methodist Hospital, Department of Pathology and Genomic Medicine, Houston, Texas 77030
[e]Cornell University, The Methodist Hospital Research Institute, Weill Cornell Medical College, NCI Center for Modeling Cancer Development, Houston, Texas 77030

Abstract. The advent of molecularly targeted therapies requires effective identification of the various cell types of non-small cell lung carcinomas (NSCLC). Currently, cell type diagnosis is performed using small biopsies or cytology specimens that are often insufficient for molecular testing after morphologic analysis. Thus, the ability to rapidly recognize different cancer cell types, with minimal tissue consumption, would accelerate diagnosis and preserve tissue samples for subsequent molecular testing in targeted therapy. We report a label-free molecular vibrational imaging framework enabling three-dimensional (3-D) image acquisition and quantitative analysis of cellular structures for identification of NSCLC cell types. This diagnostic imaging system employs superpixel-based 3-D nuclear segmentation for extracting such disease-related features as nuclear shape, volume, and cell-cell distance. These features are used to characterize cancer cell types using machine learning. Using fresh unstained tissue samples derived from cell lines grown in a mouse model, the platform showed greater than 97% accuracy for diagnosis of NSCLC cell types within a few minutes. As an adjunct to subsequent histology tests, our novel system would allow fast delineation of cancer cell types with minimum tissue consumption, potentially facilitating on-the-spot diagnosis, while preserving specimens for additional tests. Furthermore, 3-D measurements of cellular structure permit evaluation closer to the native state of cells, creating an alternative to traditional 2-D histology specimen evaluation, potentially increasing accuracy in diagnosing cell type of lung carcinomas. [DOI: 10.1117/1.JBO.17.6.066017]

Keywords: artificial intelligence; lung cancer; microscopy; non-linear diagnostic imaging; non-near optics.

Paper 12049 received Jan. 24, 2012; revised manuscript received Mar. 22, 2012; accepted for publication Apr. 24, 2012; published online Jun. 4, 2012.

1 Introduction

Lung carcinoma is the most prevalent type of cancer in the world, and it is responsible for more deaths than other types of cancer.[1] Across the globe, five-year survival rates for lung cancer patients range from 6% to 14% for men and 7% to 18% for women.[1,2] Forover 50 years, lung cancer has been viewed as a relentlessly progressive, overwhelmingly fatal disease, essentially because the utility of radiological screening remains unproven and pathologists have had only limited success in differentiating small cell from non-small cell carcinoma and staging resection specimens.[3] This has led to the use of the term non-small cell lung carcinoma (NSCLC),as a reflection of this difficulty.[3]

The 21st century has given birth to a revolution in the treatment, classification, and detection of lung cancer that promises to radically enhance survival of lung cancer patients for the first time in decades.[4] In particular, the advent of molecularly targeted therapies makes identification of the various histologic cell types and subtypes of lung cancer more important. For example, adenocarcinoma patients should be tested for epidermal growth factor receptor (EGFR) mutations as an indication of responsiveness to EGFR tyrosine kinase inhibitor.[5–7] In addition, an exclusion of a squamous cell carcinoma diagnosis is required for NSCLC patients prior to treatment with bevacizumab because of potential life-threatening hemorrhage.[8,9] As a result, additional molecular tests are frequently involved in reaching a definitive diagnosis for targeted therapies.[10,11] However, most lung carcinomas are not resected and are diagnosed and classified using small biopsies or cytology specimens.[12,13] Hematoxylin and eosin (H&E) stain of tissue sections, which is currently the gold standard for histologic diagnosis, requires hours to days for tissue transfer, processing, sectioning, and staining, and it still cannot always differentiate NSCLC cell types and subtypes. Cytology results are typically faster, but the material is even more limited in volume, and reliably separating adenocarcinoma from squamous cell carcinoma is sometimes impossible. Finally, immunochemistry may be useful in helping to make this distinction, but this method adds more time to the diagnostic process

*Authors contributed equally to this work.

Address all correspondence to: Stephen T. C. Wong, The Methodist Hospital Research Institute, Weill Cornell Medical College, Department of Systems Medicine and Bioengineering, Houston, Texas 77030. Tel: +1 7134415884; Fax: +1 7134418696; E-mail: STWong@tmhs.org.

0091-3286/2012/$25.00 © 2012 SPIE

and consumes tumor cells. Therefore, the ability to rapidly recognize different cell types and subtypes of lung cancer with minimal tissue consumption will not only facilitate the diagnostic process, but also enable maximum preservation of tissue samples for subsequent molecular testing for targeted therapy.[11] Given the risks and cost of lung biopsy, it would therefore be beneficial to develop techniques that enable fast examination of excised biopsy samples as a preliminary test for separating general cell types of lung cancer before a follow-up molecular analysis, with the aim of reducing the number of required biopsies and providing equal or greater accuracy relative to existing testing methods.

As a label-free imaging technique, CARS microscopy[14,15] holds great potential for this type of diagnostic application by significantly minimizing sampling error and realizing maximum preservation of specimen for follow-up molecular tests. By capturing intrinsic molecular vibrations to create optical contrast, CARS enables cellular imaging with submicron level spatial resolution, as well as video-speed imaging.[16–18] Two laser beams are commonly used to probe designated molecular vibrations and produce CARS emission through a four-wave mixing process.[19] Because of its high resolution and label-free imaging capability, CARS microscopy has been used to visualize various tissue structures, such as skin[20] andbrain,[21] as well as DNA backbone structures.[22] Nevertheless, to realize the diagnostic value of CARS, we must extract and analyze quantitative information from the digital CARS images in order to meet the rigorous evaluation criteria required for objective diagnosis.

Accordingly, we reported a pattern recognition and classification strategy that integrates CARS imaging with quantitative image computing techniques for cancer diagnosis.[23–27] This strategy is based on extraction and calibration of a series of pathologically related features for disease identification, thus providing meaningful diagnostic information with reproducible results. The developed platform has been successfully demonstrated using a number of disease models, including lung, breast, and prostate cancers.[23–27] In spite of this progress, the developed platform has thus far shown limited accuracy (around 70% to 75%)[25] for separation of adenocarcinoma from squamous cell carcinoma, two major cell types of NSCLC. This difficulty is not surprising and it corresponds with the clinical difficulty in differentiating these two cell types using morphology alone.[28] However, as discussed above, definitive diagnosis of these cell types is increasingly required.[29] Accordingly, we have further exploited the potential of CARS for the identification of cancer cell types by extending the previously developed two-dimensional (2-D) image analysis framework into a three-dimensional (3-D) nuclear segmentation, feature extraction, and classification system. As a nonlinear multiphoton imaging method, CARS provides superior optical sectioning capability, enabling acquisition of individual 2-D images from the same field of view but different imaging depths.[16,30] Such an image stack is usually called a z-stack. Using appropriate interpolation methods, a z-stack can be reconstructed into a 3-D volume. Throughout the remainder of the discussion, the terms z-stack and volume will be used interchangeably, as they both refer to a 3-D data structure. Such 3-D data analysis system is capable of extracting cell morphology information that accurately captures cells in their native state, thus effectively eliminating certain artificial effects posed by 2-D data analysis. For example, using 2-D data analysis, the same cell nucleus can be measured as different dimensions, depending on where the 2-D sectioning of the cell takes place. This sectioning artifact leads to confusing measurements, as a nucleus will be imaged several times, in several slices, and will have a different size in each of these slices. Taking this effect onto a whole image scale, where many cells are imaged in the same image plane. Only a small portion of these cells will be measured at the correct sizes, while the remaining cells will be measured as a different size rather than their real maximum cross-sectional dimension. We treat this effect as a sampling noise, which can hide the real size of a cell, rendering reliable analysis difficult. In contrast, a 3-D measurement would provide access to the nucleus as a whole and allow measuring real nuclear size represented by volume, potentially improving the classification accuracy between non-small cell carcinomas.

In the present work, we focus on developing a CARS-based 3-D diagnostic imaging system for nuclear segmentation and cancer cell type classification. Different mouse lung cancer models were developed by injecting human lung cancer cell lines, including adenocarcinoma and squamous cell carcinoma, as described below, into the lungs of nude mice. CARS images were acquired from normal lung tissues and different cell types of cancer lesions *ex vivo*. By stacking all image slices from one z-stack, as mentioned above, into a single data structure, a 3-D volume is formed. The generated volumes show cell nuclei as dark, roughly ellipsoidal structures surrounded by brighter cytoplasm tissues richer in CH_2 structures.

For the purpose of this study, it is imperative that the volume be automatically partitioned, or segmented, into small regions, or clusters, whose boundaries adhere to image edges as accurately as possible. If this requirement is achieved, isolating those regions containing nuclei and extracting their physical characteristics for classification become trivial tasks. This partitioning, or segmentation, could be achieved by a myriad of well-established data clustering methods that utilize image location and intensity information, such as the k-means algorithm[31] or image statistics like the expectation maximization algorithm.[32] However, these classical segmentation approaches pose a major limitation in that they minimize global energy functions, meaning they operate on the dataset as a whole and generate clusters that satisfy global conditions, which frequently results in under segmentation error.[33] Undersegmentation results in image points belonging to different objects lumped into single clusters; for example, a cluster contacting a cell nucleus will have a boundary that does not adhere to nuclear boundaries but also encompasses parts of the image background. As such, this would not be an efficient method of accurately segmenting cell nuclei, which are often too small with respect to the size of a volume. The use of a global clustering approach on such a large dataset also requires large memory capacity and computing power, a requirement that might hinder efficient execution of segmentation and follow-up diagnosis.

To circumvent these problems, superpixel-based local clustering was used to perform segmentation and generate clusters that capture real image boundaries with great accuracy in 2-D images[33] and then finally extended to 3-D images in which they are called supervoxels. We designed a modification of the simple linear iterative clustering (SLIC) algorithm to compute 3-D supervoxels.[34] Additionally, we expanded the definition of the feature vector used in clustering to include the entropy of information in 3-D volumes; this amplifies image edges and circumvents the low contrast in CARS images. In this clustering process, the 3-D volume is partitioned into small regions

based on local affinity information, and voxels are grouped into one cluster according to the similarity of their features. In this method, unlike *k*-means, a data point is not assigned to a cluster unless it falls within a small region of interest around that cluster's center. The clustered dataset is used to extract pathologically relevant features about the cell nuclei, such as volume and spatial configuration, which are then used to perform classification of lung cancer cell types.

Our results showed that the refined 3-D strategy can accurately delineate nuclear structures and has significantly improved the diagnostic accuracy between adenocarcinoma and squamous cell carcinoma. As such, these findings hold substantial potential to provide fast diagnosis with minimal tissue consumption while effectively preserving tissue specimens for follow-up molecular tests.

2 Materials and Methods

2.1 *CARS Microscopy*

The schematic of the setup was previously described.[24] One *z*-stack was imaged for each mouse, and a total of 40 (30 from tumor-bearing mice and 10 from normal control) *z*-stacks were examined. The imaging depths of these stacks range from 35 to 50 μm with 1 μm separation between images. For this study, a60x, NA1.2 water immersion objective (IR UPlanApo, Olympus, Melville, NJ) with a lateral resolution of 0.6 μm and a axial resolution of 1.5 μm was used.[35] After CARS imaging, all specimens were marked to indicate the sampled locations, sectioned through marked positions, and finally stained with H&E to be examined for the type of lesion as a standard histology control.

2.2 *Mouse Tumor Models*

Human lung cancer cell lines, A549 adenocarcinoma and NCI-H226 squamous cell carcinoma, were obtained from the American Type Culture Collection (ATCC, Manassas, VA). A549 and NCI-H69 were maintained in DMEM (Invitrogen, Grand Island, NY) medium. Both media were supplemented with 10% FCS, 100 units/mL penicillin, and 100 μg/mL streptomycin. Cancer cells were cultured in a 37 °C humidified incubator with a mixture of 95% air and 5% CO_2. All experiments were performed on exponentially growing cells with a cell population doubling time of approximately 24 to 36 h. Forty BALB/c nude mice (12-week-old females, Charles River, Wilmington, MA) were ordered for this study. Fifteen mice were assigned to each cancer group, e.g., adenocarcinoma and squamous cell carcinoma, while 10 mice were used as controls. Animals were anesthetized by Ketamine and Xylazine injection. A right posterolateral thoracic incision was made, and the thoracic wall was exposed by blunt dissection of the muscles. The tip of a 0.5-inch, 27-gauge needle was advanced by 3 mm under visual control through the translucent pleura at the third intercostal space at the dorsal midaxillary line into the pleural cavity where A549 or NCI-H226 cells (1 million/20 μL PBS) containing 1 mg/mL Matrigel (BD Biosciences, Bedford, MA) were injected. The same volume of PBS containing 1 mg/mL Matrigel without cells was injected for the control group. This group only serves as a control for the mouse tumor model but not for the diagnostic analysis. The implanted tumors were allowed to grow for two weeks before the mice were sacrificed for imaging of tumor tissues in their lungs. CARS imaging was performed close to the surface of the tumors. All processes were performed according to the guidelines of The Methodist Hospital Research Institute (TMHRI, Houston, TX).

2.3 *Image Acquisition*

Mouse lung tissues were placed on a cover slip, which was reversely placed on the chamber to keep the samples from being pressed as described in Ref. 27. The beating frequency was tuned to 2845 cm^{-1} to probe the CARS signals originating from symmetric CH_2 stretching bonds.[16] The CARS signal at around 663 nm was collected by the same objective using the backward (Epi-) detection scheme.

2.4 *Quantitative Image Analysis*

2.4.1 *Cell nucleus segmentation*

We developed a clustering and labeling pipeline based on superpixels,[36–38] which are small image patches produced by applying a clustering algorithm to localized regions of a volume. Figure 1

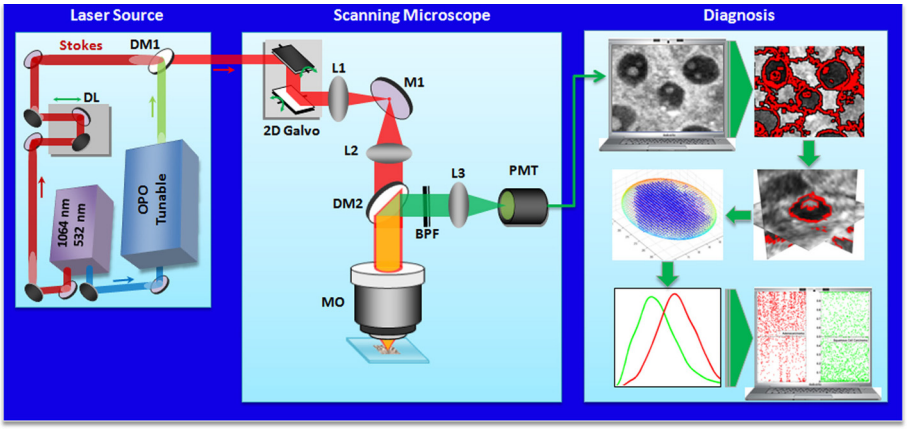

Fig. 1 Schematic illustration of the 3-D imaging, image analysis, and classification strategy. M: mirror, OPO: optical parametric oscillator, DL: delay line, DM: dichroic mirror, L: lens, MO: microscope objective, BT: breast tissue, BPF: band-pass filter, PMT: photomultiplier tube. CARS output was collected in the epi-direction. Stacking all image slices from one *z*-stack into a single data structure formed a 3-D volume. A SLIC superpixel-based local clustering approach was developed for 3-D segmentation of these nuclear structures. Segmented nuclei were then fitted with ellipsoids, enabling consistent measurements of image features related to nuclear morphology and distribution. Using these disease-related features, a classification system was developed for separation of lung cancer cell types.

shows the overall process of image segmentation, feature extraction, and classification. The benefit of superpixels lies first in their ability to capture fine image details such as edges and generate patches that adhere to natural boundaries. The boundary of a superpixel containing a cell nucleus, for example, adheres very well to the boundary of that nucleus. Second, the computational load of analysis tasks farther down the data analysis pipeline is reduced by the reduction in the number of data points, as analysis will be performed on clusters of pixels rather than individual pixels. For the remainder of this paper, the terms supervoxel and cluster carry the same meaning and are used interchangeably.

Multiple algorithms for creating superpixels exist, such as Refs. 33, 39, and 40, but the SLIC algorithm has shown superior performance in terms of segmentation errors, image boundary detection, and computational recourses.[32] SLIC operates as a modified k-means algorithm that performs clustering in a subset of clusters confined to small regions of interest in the volume, rather than partitioning datasets into k clusters to which any data point can belong. Thus, a pixel does not potentially belong to any of the k clusters, but instead to a small subset of clusters in its immediate neighborhood. In this strategy, pixels having similar characteristics are grouped together, but the limited search area ensures that pixels distant from each other, such as very similar pixels belonging to two different nuclei, are never in the same cluster. This reduces under segmentation error, and at the same time supports the assumption that later processing steps can treat a cluster as a single nucleus. Although this definition of SLIC superpixel clustering applies to datasets consisting of 2-D images, it can be easily extended to 3-D image stacks, or volumes, where data points are voxels instead of pixels. In this case, the clustering outcome is a volume partitioned into small 3-D clusters called supervoxels. In this report, we present the operation of SLIC in 3-D volumes and our extension to the feature vector used in clustering.

To perform supervoxel clustering, each voxel (v) in a volume is represented by a vector of features $f_v = [L_v, A_v, B_v, x_v, y_v, z_v, H_v]^T$ where L_v, A_v, and B_v represent CIELAB colorspace values at v. x_v, y_v, and z_v represent the coordinates of v within a volume, and H_v represents the entropy of information value at v. The entropy of a voxel is computed by calculating the entropy of the dataset represented by voxel v and all its immediate neighbors using 8-connectivity and the equation

$$H(V) = \sum_{\forall n} p(i_n) \log\ p(i_n), \tag{1}$$

where n are all the 8-connected neighbors of v, i_n is the grayscale value of a neighbor, and $p(i_n)$ is the probability of that value in the neighborhood. Entropy was added to the feature vector representing a voxel for the added reliability it provides for distinguishing edges during clustering. It can represent variability in information,[3] and, as such, it has high energy in image regions near natural edges.

Clustering was initialized by distributing cluster centers at uniform spatial intervals in the volume; the values of the feature vectors f at each cluster center served as the initial centers of those supervoxels. The algorithm searches for potential data points to associate with each cluster center based on the distance, measured as the Euclidean distance in the 7-D space of the feature vectors, between the data point and the cluster center. The search region of interest is limited to the cube whose vertices are the immediate neighboring cluster centers and the cluster center of interest at its center. For each iteration, the algorithm associates each data point to the closest cluster. At the end of an iteration, a new cluster center for each supervoxel is computed as the mean of all voxels assigned to it. Clustering terminates when the residual error computed as the sum of all $L1$ distances between new cluster centers and old cluster centers is below a preset threshold; in this study, the threshold was set at 0.2.

2.4.2 *Nucleus selection (labeling)*

Following the partitioning of the volume into supervoxels, a program with a simple user interface was created to perform labeling of those supervoxels that correspond to cell nuclei. This program operates in two repeating steps (Video 1) during which all cell nuclei can be manually selected. It is worth mentioning that labeling is an efficient process, as labeling an entire $512 \times 512 \times 80$ volume consumes about five min.

2.4.3 *Classification and diagnostic analysis*

Thus far, the focus has been on sifting through a very large dataset of three-dimensional images to find a small subset of data that contains information relevant to diagnosis, namely the voxels corresponding to cell nuclei. Hereafter this subset of data is used to compute physical features that contain enough information to represent the cell nuclei and build a classifier that can perform automatic identification of cancer cell types.

To ensure consistency in extracted features across different volumes, we assumed a cell nucleus to be roughly ellipsoidal in shape, and, as such, an ellipsoid was fitted to each contiguous set of 3-D points representing a nucleus. The features we used for each nucleus were the physical features of the ellipsoid that best fitted the convex hull of the points comprising that nucleus; in other words, the ellipsoid that best fitted the smallest region in space that could enclose all the points comprising a nucleus. Computed features were the volume and the lengths of the major and minor axes of the fitted ellipsoid. Furthermore, features representing the spatial position of a nucleus relative to its neighbors were computed to incorporate information about the distribution of cell structures. We constructed the Delaunay

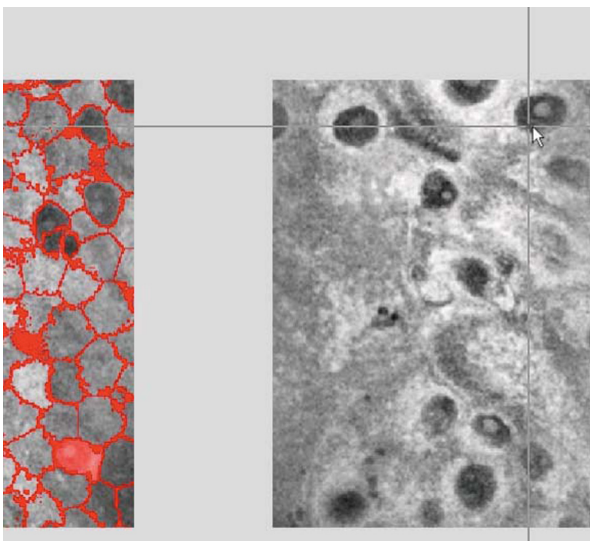

Video 1 Demonstration of nuclear labeling process. (MOV, 3.7 MB) [URL: http://dx.doi.org/10.1117/1.JBO.17.6.066017.1]

triangulation[41–43] to define the connectivity of nuclei in the sample. Using the triangulation, four features were computed for each nucleus, including the distance to the farthest neighbor, distance to the nearest neighbor, mean distance to neighbors, and orientation relative to the nearest neighbor. These distances were respectively represented by: the length of the longest edge of the Delaunay triangulation structure attached to the nucleus of interest, the length of the shortest Delaunay edge attached to the nucleus, the average length of all Delaunay edges attached to a nucleus, and the angle between the major axis of a cell and the major axis of its nearest neighbor.

We performed segmentation, labeling, and feature extraction from 15 volumes corresponding to adenocarcinoma and another 15 volumes from squamous cell carcinoma. In addition, because we wanted to demonstrate the superiority of information extracted in three dimensions over that extracted from two dimensions, we used three slices from each image stack and extracted the same features from those to serve as a 2-D benchmark. It is worthnoting that all features can be mapped to any dimension, e.g., an ellipsoid mapped to two dimensions becomes an ellipse; volume becomes area. The major difference between 3-D and 2-D representation of the features is that an ellipse has only two equatorial radii, one major and one minor axis, as opposed to an ellipsoid that has three such radii. Compared to 2-D, 3-D measurements resulted in one more feature as minor axis length since there are three axes in a 3-D ellipsoid.

Since each volume was identified by the statistics of its features, mean, standard deviation, skewness, and kurtosis of the distribution function were calculated for each of the seven (in 2-D) or eight (in 3-D) features in a given volume. These quantities constituted the 32 features used to build a classifier capable of characterizing a volume as either an adenocarcinoma or squamous cell carcinoma cell type. The leave-one-out approach, also used for differential diagnosis of lung carcinoma cell types by Ref. 24, was utilized to demonstrate that the designated statistical features could be used to perform automatic diagnosis. We detail this method through the following example. If samples from each cell type were labeled 1 through 15, A1 through A15 for adenocarcinoma samples and S1 through S15 for squamous cell carcinoma, samples A1 and S1 would be excluded on the first iteration, and the remaining 28 samples would be used to train the a classifier, with the two excluded samples (A1 and S1) used to validate that classifier through testing whether it can assign them to their correct subtype. On the second iteration, sample A1 would be left out with sample S2, and the training/model testing process is repeated. This process is repeated over enough iterations to exhaust all possible parings of excluded samples. As a benchmark in this study, the process was performed both in 2-D and in 3-D datasets.

3 Results

3.1 *CARS Images of Different Types of Lung Cancers*

Figure 2 shows representative CARS images and corresponding H&E results of normal lung tissue and two cell types of non-small cell lung cancers. Tissue structures were clearly identified on the cellular level. The normal lung tissue sample is predominantly composed of well-organized fibrous and matrix structures, consisting of the bronchi and supporting matrix for alveoli [Fig. 1(a) and 1(b)]. Cancerous regions showed much denser cellularity compared with normal regions, and the size

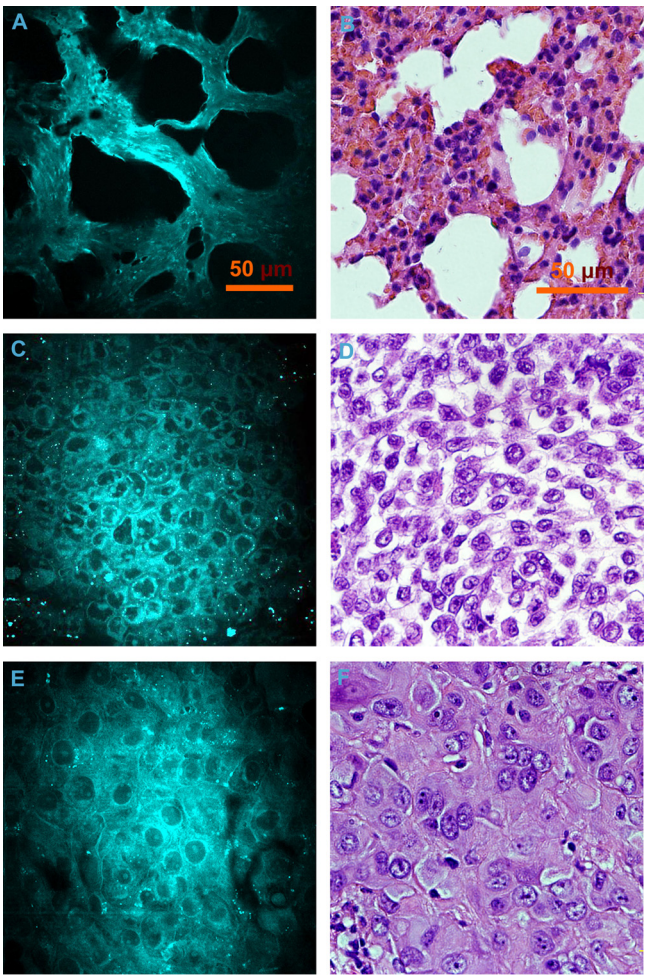

Fig. 2 CARS images of mouse lung tissues taken at Raman shift of 2845 cm^{-1} and their corresponding H&E stained images: (a) (b) normal lung, (c) (d) adenocarcinoma and (e) (f) squamous cell carcinoma derived from the same mouse, respectively. Scale bars: 50 μm.

and configuration of the cells corresponded with these parameters, as shown by H&E staining [Fig. 1(c) through 1(h)]. Commonly used pathological features were also identified for individual cell types of cancers, including vesicular nuclei, prominent and moderately abundant foamy cytoplasm[44] for adenocarcinoma [Fig. 1(c) and 1(d)], and pleomorphic malignant cells containing keratin with abundant cytoplasm and formation of intracellular bridges[45] for squamous cell carcinoma [Fig. 1(e) and 1(f)].

3.2 *Segmentation and Labeling of 3-D Volumes*

Segmentation of each volume, or z-stack, resulted in new volume data, which were partitioned, or segmented, into supervoxels. For all subsequent processing steps, we considered a supervoxel to represent one data point. This is possible based on the assumption that a well-performing clustering algorithm will generate supervoxels in which all individual voxels belong to the same class. Indeed, as illustrated by Fig. 3, all voxels in a supervoxel only represent either cell nuclei or background. A sample slice of a segmented volume is presented in Fig. 3(a), and the same slice after clustering is shown in Fig. 3(b). The red regions represent the boundaries of supervoxels. The boundaries in certain regions appear as surfaces rather than

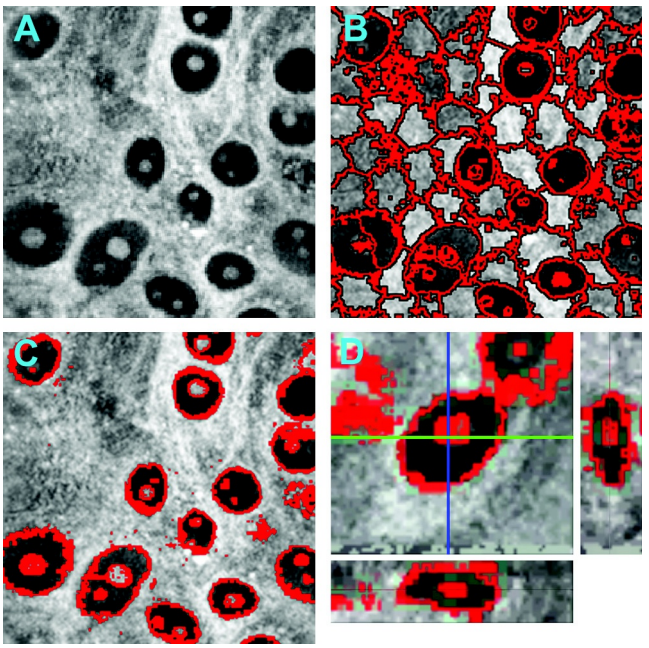

Fig. 3 Superpixel-based 3-D nuclear segmentation process. A sample slice of a volume is presented (a), where all voxels in a supervoxel represent either cell nuclei or backgrounds. The same slice after clustering is shown (b), in which the red regions represent the boundaries of supervoxels. (c) shows the outcome of labeling the clustered volume where the boundaries of the labeled supervoxels accurately capture the boundaries of cell nuclei. The 3-D segmented structure of a cell nucleus is illustrated in (d). The *YZ* and *XZ* cross sections are presented in the right and bottom panels, which were constructed from the depth stack along the blue and green lines, respectively.

lines because the chosen slice passes through the boundary of the 3-D supervoxel. It is notable that those supervoxels enclosing nuclei are completely separable from those enclosing background and that supervoxel boundaries accurately capture nuclear boundaries. It is this preliminary segmenting of the volume into clusters belonging to either nuclei or background that allowed us to proceed to the next step in the image analysis framework, namely, labeling of those supervoxels that represent nuclei. Figure 3(c) further shows the outcome of labeling the clustered volume where the boundaries of the labeled supervoxels accurately capture the boundaries of the nuclei, while the 3-D boundary of a representative cell nucleus is illustrated in Fig. 3(d). It is worth mentioning that an accurate boundary was determined in all three dimensions as a result of a smooth segmentation process. Video 2 shows representative reconstructed nuclei after segmentation in a whole squamous cell carcinoma volume.

3.3 *Diagnostic Analysis of Lung Cancer Cell Types*

As described in the Methods section and shown in Fig. 3(c) and 3(d), the segmented cell nuclei were fitted with ellipsoids for consistent extraction of feature information. Figure 4 illustrates a representative case of the fitting results on all the nuclei in a squamous cell carcinoma volume, where all ellipsoids are plotted with their color representing different depths within the z-stack. This mesh in Fig. 4 is representative of the real size and distribution of nuclei within the imaged tissue, and it was used to extract pathologically relevant information, namely, the features defined in the Methods section, to be utilized in automatic differential diagnosis. As such, the above-

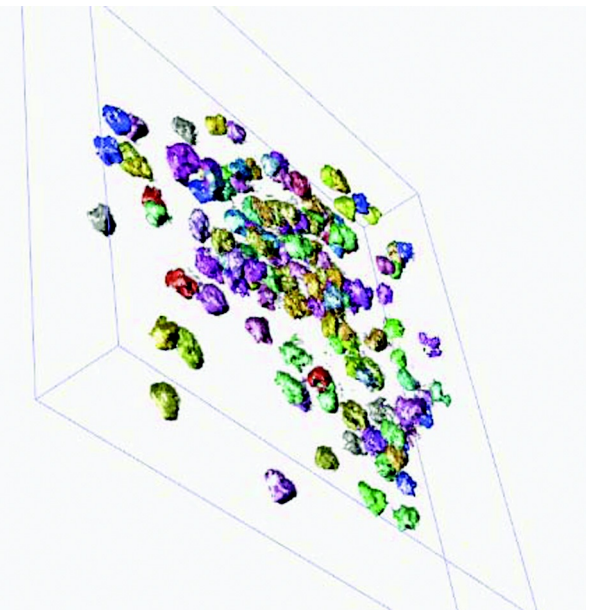

Video 2 Reconstructed cell nuclei in a whole squamous cell carcinoma volume. (MOV, 3.5 MB) [URL: http://dx.doi.org/10.1117/1.JBO.17.6.066017.2]]

defined features were measured across different volumes consistently following the same procedure. Since multiple cell nuclei existed in each volume (Figs. 3 and 4), the measurement resulted in a probability distribution function (PDF) for each measured feature in a given volume. We found that distributions of five out of eight measured features showed significant difference between 2-D and 3-D measurements using data from all studied volumes through both 2-D and 3-D computation (Fig. 5).They were mostly related to the size, shape, and orientation of nuclear structures. We note here that features related to nuclear size and shape failed to show a clear separation between the two cancer cell types in 2-D measurements [Fig. 5(a) through 5(c)]. In contrast, 3-D measurements effectively captured the difference between the two cell types by showing clear separations of their peak positions [Fig. 5(e) through 5(g)]. While nuclear orientation shows a clear peak with 2-D measurement [Fig. 5(d)], this peak turns into an even distribution across different angles in 3-D [Fig. 5(h)]. The presented PDF curves were estimated from the measured data, i.e., they represent the histograms of the features processed with a smoothing kernel causing the curves in some cases to have tails in the negative side of the number line. Measurements related to the remaining three feature distributions, which carry information on the distance between individual cell nuclei, failed to show clear separations between cancer cell types both in 2-D and 3-D data and thus are not illustrated here.

Using the calculated features, a classifier was built, as described in the Methods section, and classification was performed to separate cancer cell types. Figure 6 and Table 1 illustrate the automatic classification results. In Fig. 6(a) and 6(b), results of classification using 2-D data are presented, where each point represents one tissue sample, specifically the one that was left out during a particular iteration. The threshold for classification is the straight line $y = 0.5$. Points with $y \geq 0.5$ were classified as adenocarcinoma, while points with $y < 0.5$ were classified as squamous cell carcinoma. For better presentation, the graph is separated into two separate subfigures, respectively

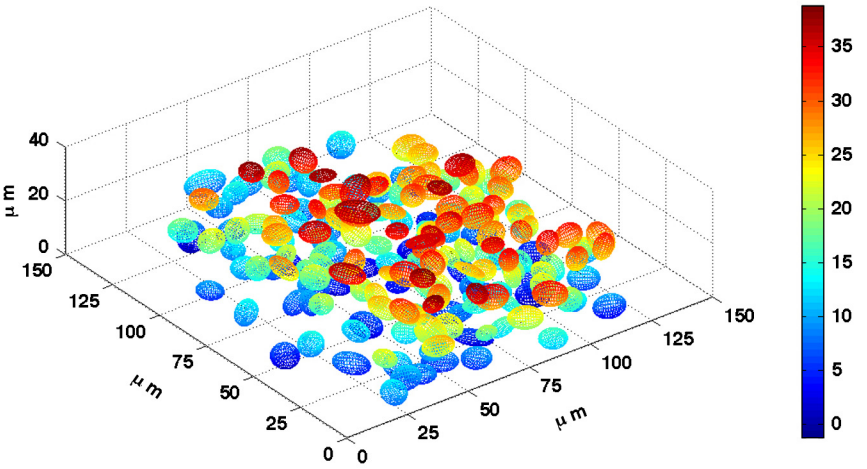

Fig. 4 3-D nuclear distribution of a squamous cell carcinoma volume after supervoxel-based nuclear segmentation. All ellipsoids are plotted with their color representing different depths within the volume.

representing adenocarcinoma samples [Fig. 6(a)] and squamous cell carcinoma samples [Fig. 6(b)]. Classification from 2-D data resulted in a true positive rate of 71.98% and 65.05% for adenocarcinoma and squamous cell carcinoma, respectively (Table 1). False positive rate, in the same order, was 28.02% and 34.95%. Classification results from the 3-D data analysis are plotted in Fig. 6(c), where clear separation between cell types allows for data visualization on the same graph. As shown in Table 1, quantified classification accuracies were a 99.56% and 97.78% true positive rate for adenocarcinoma and squamous cell carcinoma, respectively. False positive classification was 0.45% and 2.22% in the same order. The results showed that features extracted from 3-D data analysis provided information that significantly enhanced the classification accuracy and thus demonstrated proof of concept that information extracted from 3-D image analysis and segmentation can be used for the automatic diagnosis of lung cancer subtypes.

4 Discussion

Rapid advances in optical imaging technologies have led to substantial contributions to advancing diagnostic strategies and improving care delivery in cancer research. To exploit the diagnostic value of acquired images for clinical diagnosis, an effective imaging and image analysis platform should be developed to allow accurate evaluation of imaging data in a repeatable manner. Thus far, several studies have explored the diagnostic potential of CARS,[23–27] promoting the translation of this label-free technique for clinical use. These strategies were based on extraction and calibration of a series of disease-related morphology features for diagnosis. From this, the CARS technique has been successfully bridged to clinical evaluations. However, similar to the commonly used H&E stain technique, the morphology-based classification system encounters difficulties in distinguishing certain diseases, such as separation of the cell types of NSCLC. The problem originates from the fact that these cancer cell types often show a similar morphology, especially in poorly differentiated areas, preventing accurate characterization.

Taking aim at this problem, this study proposed a strategy to increase the accuracy of NSCLC characterization by extending 2-D analytical strategies to a 3-D analytic platform. By taking advantage of the optical sectioning capability provided by CARS, our strategy allows analysis of cellular features in 3-D, a setting closer to the microenvironment in which the cells reside. As illustrated in Fig. 5, five of the eight disease-related features (volume, major axis length, lengths of the two minor axes, and the orientation relative to the nearest neighbor) showed clear separation in 3-D measurements when compared to their four equivalent features from the 2-D benchmark.

In this strategy nuclear volume was first measured in 3-D to provide size information. As discussed in the introduction, this effectively allowed suppression of the sampling error posed by measurements from 2-D slices. As a result, a clear separation of adenocarcinoma from squamous cell carcinoma was observed. In contrast, the 2-D analysis showed much broader distributions for both cell types without clear separation of peak positions, potentially caused by the sampling noise. Second, the sampling error in 2-D also obscured identification of the nuclear size difference between examined cell types. It is worth mentioning that the peaks of the major axis lengths of adenocarcinoma and squamous cell carcinoma were about 6 and 5.5 μm [Fig. 5(f)], respectively. Although they were well separated in 3-D measurements, 2-D measurements of the same parameter did not show a clear difference. More importantly, both cell types showed the peak value of major axis length between 4 and 5 μmin 2-D [Fig. 5(b)], values that were substantially smaller than the resulting values in 3-D. These data strongly indicated that such 2-D measurements combined values associated with both sampling noise and real axis lengths. Specifically, if, in a given plane, we assume that all cell nuclei have the same axis length, then the measured axis length for a given nucleus can range from zero to its actual length, depending on the selection of the plane. This effect is true for every cell nucleus in that plane, resulting in a distribution of the measured value from zero to the actual length, especially when the spatial locations of individual nuclei are unrelated. As such, a sampling noise is created that lowers the peak position of the distribution curve away from the real value and also broadens the distribution curve if there are variations in the axis length among individual nuclei [Fig. 5(b)]. In contrast, 3-D measurement of the same parameter resulted in much narrower curves with clear separation of peak positions.

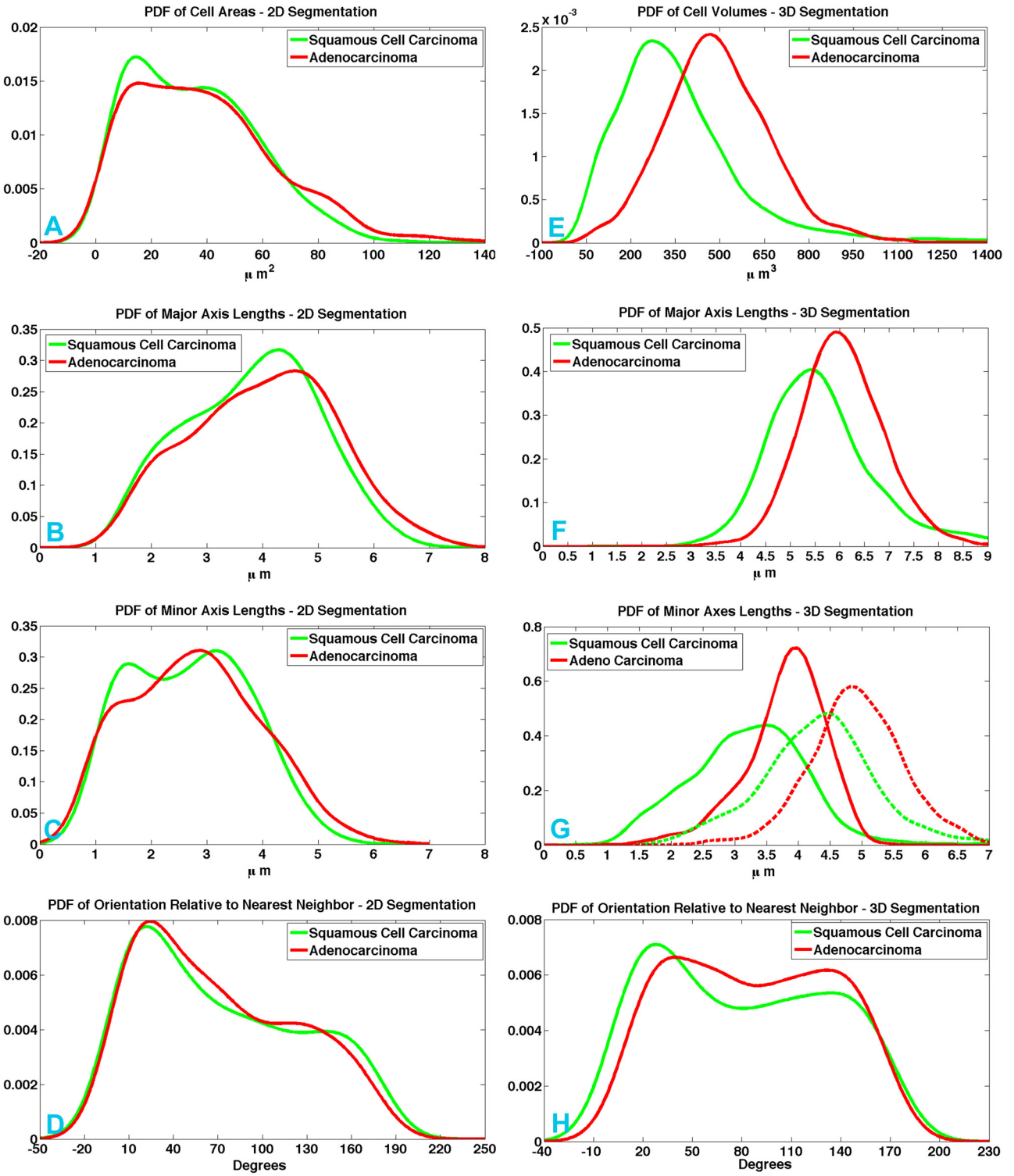

Fig. 5 Distribution of four representative features extracted from the segmentation results. PDF curves are fitted to the distributions to illustrate the data structure. Left panels, (a) through (d), show results from 2-D segmentation, while right panels, (e) through (h), show results from 3-D segmentation. Data from adenocarcinoma and squamous cell carcinoma are plotted in red and green, respectively.

The same observation was supported by minor axis lengths, as well [Figs. 5(c) and 5(g)]. Third, the relative orientation angle between neighbors showed a broad peak around 25 deg [Fig. 5(d)]. This peak was weakened in the 3-D results [Fig. 5(h)], where a more even distribution was observed across the spectrum of all angles, indicating a lack of orientation in such tumors. This distribution could be caused by the use of animal models, instead of human tumor samples, as it is well-known that adenocarcinomas tend to form glandular structures, while squamous cell carcinomas tend to form well-oriented cell sheets.[45,46] Consequently, by showing more random cellular distribution patterns, the mouse tumor model could be more poorly differentiated compared to human tumors. Cell lines also tend to be relatively poorly differentiated, since

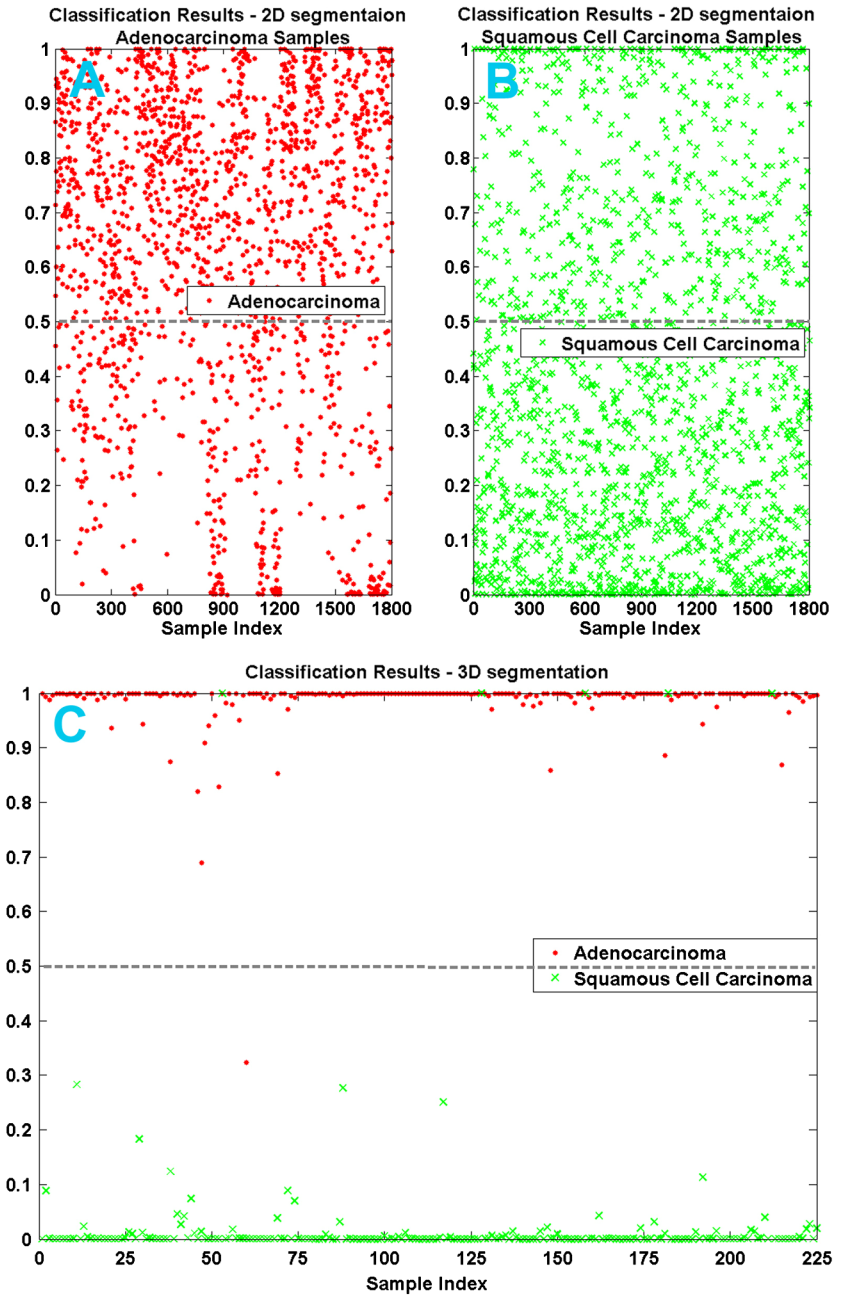

Fig. 6 Visualization of 2-D and 3-D classification results. (a) and (b) present adenocarcinoma and squamous cell carcinoma results with 2-D data analysis, respectively. Each point represents one tissue sample. The threshold for classification is the straight line $y = 0.5$. Points with $y \geq 0.5$ were classified as adenocarcinoma while points with $y < 0.5$ were classified as squamous cell carcinoma. Similarly, classification results from the 3-D data analysis are plotted (c), where clear separation between cell types allows for data visualization on the same graph.

these tumors tend toward immortalization. We therefore expect a much more prominent difference of their PDF curves in human tumors, especially when measured in 3-D. In another sense, this difference also supports the utility of the 3-D approach since this method even worked well on mouse models, which are harder to separate. However, the tremendous heterogeneity of human tumors, as compared with only two cell lines in this study, may pose challenges for classification that are difficult to capture in this model system. Finally, compared to the aforementioned features, a clear distinction between 2-D and 3-D approaches could not be found relative to measurements of distance-related features. This was expected because the sampling noise posed by 2-D does not affect the center position of cell nuclei, which are the major determinants of cell-cell distance.

With increasing attention to development of CARS-based microendoscopy to support label-free, *in vivo*, molecular diagnosis,[47–52] another benefit of the proposed 3-D image quantitation system lies in its potential for *in vivo* differentiation of lung carcinoma cell types and possibly subtypes during biopsy. Specifically, it has long been known that most lung cancers are histologically heterogeneous and that most adenocarcinomas have more than one histologic subtype.[44] With the advent of molecularly targeted therapies, avoiding sampling errors to allow complete identification of the various histologic cell

Table 1 2-D and 3-D classification results.

2-D/3-D	Adenocarcinoma	Squamous cell carcinoma
Adenocarcinoma	71.98%/99.56%	34.94%/0.45%
Squamous cell carcinoma	28.02%/2.22%	65.05%/97.78%

types and subtypes within a given lung cancer becomes even more important. CARS allows selecting biopsy sites within a mass or nodule to minimize sampling error. Blind aspiration biopsy or fluoroscopic guided biopsy may sample surrounding tissues rather than the cancer and may not sample different cell types or subtypes within a cancer; thus, they may not be representative of the cancer as a whole. This is particularly important for targeted therapy since any adenocarcinoma component may respond to EGFR tyrosine kinase inhibitor therapy, but the adenocarcinoma component may not be sampled in a mixed cancer, such as an adenosquamous carcinoma, using current techniques. Reducing sampling error improves the accuracy of obtaining tissue and increases the useful sample size for biomarker testing. Since adenocarcinoma subtypes are associated with different biomarkers, future research into CARS microscopy could greatly enhance complete sampling of the different subtypes within an adenocarcinoma. It will not only ensure sampling of all cell types and subtypes within a heterogeneous lung cancer for molecular analysis at the time of biopsy, but also facilitate the whole diagnostic process while providing more abundant biopsy samples of the correct tissues for biomarker studies.

In conclusion, we demonstrated a 3-D analytical strategy in conjunction with the CARS imaging technique for fast and accurate determination of NSCLC cell types. By stacking multiple image slices from a z-stack into a single data structure, 3-D nuclear segmentation, labeling, and measurements were realized for extraction of disease-related features using SLIC-based supervoxel segmentation. Classification was then performed using the extracted features. Compared to a 2-D approach, the 3-D strategy showed much higher efficacy with greater than 97% accuracy and specificity for separation of NSCLC cell types. Collectively, this strategy effectively takes advantage of the superior optical sectioning capability of the CARS technique; meanwhile, it enables quantification of image features in a configuration closer to the natural arrangement of tissues. By doing so, a significant accuracy improvement was achieved for separation of lung cancer subtypes. In addition, since no tissue consumption or sectioning was required, the combination of CARS and the 3-D analytical approach offers an alternative strategy to the widely used H&E staining technique for lesion evaluation with faster analysis times. Therefore, the developed 3-D diagnostic platform promises to provide a new modality that combines advanced nonlinear optical imaging methods with quantitative bioinformatics techniques for label-free delineation of tissue pathology, thus holding the potential to facilitate diagnosis while effectively preserving tissue specimens for follow-up diagnostic tests.

Acknowledgments

We would like to thank Drs. Kelvin K. Wong, Hong Zhao, Kemi Cui and Zhong Xue from Department of Systems Medicine and Bioengineering, The Methodist Hospital Research Institute for helpful discussions. The funding of this research was initiated and supported by the Department of Systems Medicine and Bioengineering, TMHRI, Weill Cornell Medical College, and the TT & WF Chao Foundation and John S. Dunn Research Foundation to STCW. Provisional patent filed.

References

1. D. M. Parkin et al., "Global cancer statistics, 2002," *Ca-Cancer J. Clin.* **55**(2), 74–108 (2005).
2. D. R. Youlden, S. M. Cramb, and P. D. Baade, "The international epidemiology of lung cancer: geographical distribution and secular trends," *J. Thorac. Oncol.* **3**(8), 819–831 (2008).
3. P. S. Shenkin, B. Erman, and L. D. Mastrandrea, "Information-theoretical entropy as a measure of sequence variability," *Proteins* **11**(4), 297–313 (1991).
4. P. T. Cagle et al., "Revolution in lung cancer: new challenges for the surgical pathologist," *Arch. Pathol. Lab. Med.* **135**(1), 110–116 (2011).
5. M. Maemondo et al., "Gefitinib or chemotherapy for non-small-cell lung cancer with mutated EGFR," *N. Engl. J. Med.* **362**(25), 2380–2388 (2010).
6. T. Mitsudomi et al., "Gefitinib versus cisplatin plus docetaxel in patients with non-small-cell lung cancer harbouring mutations of the epidermal growth factor receptor (WJTOG3405): an open label, randomised phase 3 trial," *Lancet Oncol.* **11**(2), 121–128 (2010).
7. T. S. Mok et al., "Gefitinib or carboplatin-paclitaxel in pulmonary adenocarcinoma," *N. Engl. J. Med.* **361**(10), 947–957 (2009).
8. M. H. Cohen et al., "FDA drug approval summary: bevacizumab (Avastin) plus Carboplatin and Paclitaxel as first-line treatment of advanced/metastatic recurrent nonsquamous non-small cell lung cancer," *Oncologist* **12**(6), 713–718 (2007).
9. D. H. Johnson et al., "Randomized phase II trial comparing bevacizumab plus carboplatin and paclitaxel with carboplatin and paclitaxel alone in previously untreated locally advanced or metastatic non-small-cell lung cancer," *J. Clin. Oncol.* **22**(11), 2184–2191 (2004).
10. P. S. Loo et al., "Subtyping of undifferentiated non-small cell carcinomas in bronchial biopsy specimens," *J. Thorac. Oncol.* **5**(4), 442–447 (2010).
11. W. D. Travis et al., "International association for the study of lung cancer/American thoracic society/European respiratory society international multidisciplinary classification of lung adenocarcinoma," *J. Thorac. Oncol.* **6**(2), 244–285 (2011).
12. C. I. Henschke, "Early lung cancer action project: overall design and findings from baseline screening," *Cancer* **89**(S11), 2474–2482 (2000).
13. F. Levi et al., "Trends in mortality from major cancers in the European Union, including acceding countries, in 2004," *Cancer* **101**(12), 2843–2850 (2004).
14. M. D. Duncan, J. Reintjes, and T. J. Manuccia, "Imaging biological compounds using the coherent anti-Stokes Raman scattering microscope," *Opt. Eng.* **24**, 352–355 (1985).
15. M. D. Duncan, J. Reintjes, and T. J. Manuccia, "Scanning coherent anti-Stokes Raman microscope," *Opt. Lett.* **7**, 350–352 (1982).
16. C. L. Evans and X. S. Xie, "Coherent anti-Stokes Raman scattering microscopy: chemical imaging for biology and medicine," *Annu. Rev. Anal. Chem.* **1**, 883–909 (2008).
17. C. L. Evans, E. O. Potma, and X. S. Xie, "Coherent anti-Stokes Raman scattering spectral interferometry: determination of the real and imaginary components of nonlinear susceptibility chi(3) for vibrational microscopy," *Opt. Lett.* **29**(24), 2923–2925 (2004).
18. M. Muller and A. Zumbusch, "Coherent anti-Stokes Raman scattering microscopy," *ChemPhysChem* **8**(15), 2156–2170 (2007).
19. J.-X. Cheng and X. S. Xie, "Coherent anti-Stokes Raman scattering microscopy: instrumentation, theory, and applications," *J. Phys. Chem. B* **108**(3), 827–840 (2004).
20. C. L. Evans et al., "Chemical imaging of tissue in vivo with video-rate coherent anti-Stokes Raman scattering microscopy," *Proc. Natl. Acad. Sci. USA* **102**(46), 16807–16812 (2005).
21. C. L. Evans et al., "Chemically-selective imaging of brain structures with CARS microscopy," *Opt. Express* **15**(19), 12076–12087 (2007).

22. J. X. Cheng et al., "Laser-scanning coherent anti-Stokes Raman scattering microscopy and applications to cell biology," *Biophys. J.* **83**(1), 502–509 (2002).
23. Y. Yang et al., "Differential diagnosis of breast cancer using quantitative, label-free and molecular vibrational imaging," *Biomed. Opt. Express* **2**(8), 2160–2174 (2011).
24. L. Gao et al., "On-the-spot lung cancer differential diagnosis by label-free, molecular vibrational imaging and knowledge-based classification," *J. Biomed. Opt.* **16**(9), 096004 (2011).
25. L. Gao et al., "Diagnosing lung cancer using coherent anti-Stokes Raman scattering microscopy," in *Proc. SPIE* **7890**, 789015 (2011).
26. L. Gao et al., "Label-free high-resolution imaging of prostate glands and cavernous nerves using coherent anti-Stokes Raman scattering microscopy," *Biomed. Opt. Express* **2**(4), 915–926 (2011).
27. Y. Yang et al., "Label-free imaging of human breast tissues using coherent anti-Stokes Raman scattering microscopy," *Proc. SPIE* **7903**, 79032G (2011).
28. J. Terry et al., "Optimal immunohistochemical markers for distinguishing lung adenocarcinomas from squamous cell carcinomas in small tumor samples," *Am. J. Surg. Pathol.* **34**(12), 1805–1811 (2010).
29. C. J. Langer et al., "The evolving role of histology in the management of advanced non-small-cell lung cancer," *J. Clin. Oncol.* **28**(36), 5311–5320 (2010).
30. W. Denk, J. H. Strickler, and W. W. Webb, "Two-photon laser scanning fluorescence microscopy," *Science* **248**(4951), 73–76 (1990).
31. J. Hartigan and M. Wong, "Algorithm AS 136: aK-means clustering algorithm," *J. Royal Stat. Soc. C (Appl. Stat.)* **28**(1), 100–108 (1979).
32. T. Moon, "The expectation-maximization algorithm," *IEEE Signal Process. Mag.* **13**(6), 47–60 (1996).
33. R. Achanta et al., "Slic superpixels," Technical Report 149300 EPFL (2010).
34. A. Lucchi et al., "Supervoxel-based segmentation of EM image stacks with learned shape feature," in EPFL TECHNICAL REPORT (2010).
35. Z. Wang et al., "Delivery of picosecond lasers in multimode fibers for coherent anti-Stokes Raman scattering imaging," *Opt. Express* **18**(12), 13017–13028 (2010).
36. X. Ren and J. Malik, "Learning a classification model for segmentation," in *Ninth IEEE Int. Conf. on Computer Vision*, Nice, France, p. 10, Springer-Verlag, Berlin, Heidelberg (2003).
37. A. A. Hammoudi et al., "Automated nuclear segmentation of coherent anti-Stokes Raman scattering microscopy images by coupling superpixel context information with artificial neural networks," in *Proc. Second Int. Conf. on Machine Learning in Medical Imaging*, Toronto, Canada, Springer-Verlag (2011).
38. A. Radhakrishna et al., "SLIC Superpixels," Technical Report 149300, EPFL (June, 2010).
39. A. Levinshtein et al., "Turbopixels: fast superpixels using geometric flows. Pattern analysis and machine intelligence," *IEEE Trans. Pattern Anal. Mach. Intell.* **31**(12), 2290–2297 (2009).
40. X. Ren and J. Malik, "Learning a classification model for segmentation," In: "*Computer Vision*" in *Proc. Ninth IEEE Int. Conf.*, pp. 10–17 (2003).
41. Y. Xu et al., "Capacity-constrained Delaunay triangulation for point distributions," *Comput. Graph.* **35**(3), 510–516 (2011).
42. F. Li et al., "Multiple nuclei tracking using integer programming for quantitative cancer cell cycle analysis," *IEEE Trans. Med. Imag.* **29**(10), 96–105 (2010).
43. F. Li, X. Zhou, and T. C. S. Wong, "Optimal live cell tracking for cell cycle study using time-lapse fluorescent microscopy images," in *Int. Workshop on Machine Learning in Medical Imaging (MLMI 2010)*, pp. 124–131, Springer Lecture Notes in Computer Science, Beijing, China (2010).
44. A. Laga et al., "Adenocarcinoma," in *Color Atlas and Text of Pulmonary Pathology*, 2nd ed., pp. 31–41, Lippincott Williams & Wilkins, Philadelphia, PA (2008).
45. E. Zeren et al., "Squamous-cell carcinoma," in *Color Atlas and Text of Pulmonary Pathology*, 2nd ed., pp. 42–46, Lippincott Williams & Wilkins, Philadelphia, PA (2008).
46. V. Kumar et al., Eds., *Pathologic Basis of Disease*, 8th ed., Saunders, Philadelphia, PA (2009).
47. B. G. Saar et al., "Coherent Raman scanning fiber endoscopy," *Opt. Lett.* **36**(13), 2396–2398 (2011).
48. M. Balu et al., "Fiber delivered probe for efficient CARS imaging of tissues," *Opt. Express* **18**(3), 2380–2388 (2010).
49. F. Legare et al., "Towards CARS Endoscopy," *Opt. Express* **14**(10), 4427–4432 (2006).
50. Z. Wang et al., "Coherent anti-Stokes Raman scattering microscopy imaging with suppression of four-wave mixing in optical fibers," *Opt. Express* **19**(9), 7960–7970 (2011).
51. Z. Wang et al., "Use of multimode optical fibers for fiber-based coherent anti-Stokes Raman scattering microendoscopy imaging," *Opt. Lett.* **36**(15), 2967–2969 (2011).
52. Z. Wang et al., "Delivery of picosecond lasers in multimode fibers for coherent anti-Stokes Raman scattering imaging," *Opt. Express* **18**(12), 13017–13028 (2010).